University of Kentucky

UKnowledge

A method for phenotyping roots of large plants

Brian Rinehart
University of Kentucky

Hanna J. Poffenbarger
University of Kentucky

Daniel Lau
University of Kentucky

David H. McNear
University of Kentucky

Follow this and additional works at: https://uknowledge.uky.edu/pss_facpub

Part of the Plant Sciences Commons, and the Soil Science Commons

Right click to open a feedback form in a new tab to let us know how this document benefits you.

Repository Citation

A method for phenotyping roots of large plants

SPECIAL SECTION: BELOWGROUND PHENOTYPING

A method for phenotyping roots of large plants

Brian Rinehart[1] | **Hanna Poffenbarger[1]** | **Daniel Lau[2]** | **Dave McNear[3]**

[1] Agroecosystem Nutrient Cycling Laboratory, Dep. of Plant and Soil Sciences, Univ. of Kentucky, Lexington, KY, USA

[2] Dep. of Engineering, Univ. of Kentucky, Lexington, KY, USA

[3] Rhizosphere Science Laboratory, Dep. of Plant and Soil Sciences, Univ. of Kentucky, Lexington, KY, USA

Correspondence
Dave McNear, Rhizosphere Science Laboratory, Dep. of Plant and Soil Sciences, Univ. of Kentucky, Lexington, KY, USA.
Email: dave.mcnear@uky.edu

Assigned to Associate Editor Saoirse Tracy.

Funding information
USDA National Institute of Food and Agriculture, Grant/Award Number: 2019-67019-29401; a cooperative agreement with the Kentucky Agricultural Experiment Station (KY006117), and the University of Kentucky Department of Plant and Soil Sciences.

Abstract
Linking root traits to plant functions can enable crop improvement for yield and ecosystem functions. However, plant breeding efforts targeting belowground traits are limited by appropriate phenotyping methods for large root systems. While advances have been made allowing for imaging large in situ root systems, many of these methods are inaccessible due to expensive technology requirements. The aim of this work was to develop a plant phenotyping platform and analysis method suitable for assessing root traits of large, intact root systems. With the use of a purpose-built imaging table and automated photo capture system, machine learning-based image segmentation, and off-the-shelf trait analysis software, the developed method yielded results of comparable accuracy to commercial root scanning platforms without requiring access to prohibitively expensive equipment. This methodology enables root studies to move beyond the size limitations of scanner-based methods, integrate whole-system traits like root depth distribution, and save time on root image capture.

1 | INTRODUCTION

Root system architecture, morphology, and chemistry are suites of root traits—understood in this paper as measurable, genetically determined characteristics of plant roots—that influence a wide range of plant and ecosystem functions (Freschet, Roumet, et al., 2020). These include nutrient uptake (Fletcher et al., 2020; Guo & York, 2019),

Abbreviations: DI, deionized; DSLR, digital single-lens reflex; GUI, graphical user interface; LAURIS, LAURootImagingSystem; MBE, mean bias error; nRMSE, normalized root mean square error; PVC, polyvinyl chloride; R2, coefficient of determination; RAM, random access memory; RANSAC, random sample and consensus algorithm; RMSE, root mean square error; TIFF, Tag Image File Format.

water uptake (Comas et al., 2013), nutrient cycling (Man et al., 2020; Moore et al., 2020; Phillips et al., 2011), and soil carbon storage (Poirier et al., 2018; Rossi et al., 2020). Because breeding for specific root traits could lead to improvements in crop efficiencies and ecosystem services (McGrail et al., 2020; Tracy et al., 2020), there is a growing interest in understanding variation in root traits. Indeed, per Web of Science (Thomson Reuters), publications related to root phenotyping and selection for belowground traits increased five-fold between 2000 and 2020. However, recovering intact root systems from soils is a significant challenge, and root-based phenotyping and breeding efforts remain constrained by the limited phenotyping technologies and methodologies available (Downie et al., 2015; McCormack

et al., 2017; Paez-Garcia et al., 2015; Reynolds et al., 2021; Topp et al., 2016).

One area needing improvement, and the focus of this article, is the imaging and analysis of large, intact root systems. One reason for this is that many phenotyping approaches rely on imaging seedlings, but there is uncertainty about how well root traits in young plants correspond to traits in more developed plants (Rich et al., 2020). In addition, some field-based root measurement techniques for larger plants, such as "shovelomics" (Trachsel et al., 2011) and soil coring, measure only portions of the root systems and use models to extrapolate to the whole system (Paez-Garcia et al., 2015). These models can be improved using measurements of whole systems taken at multiple developmental stages (McCormack et al., 2017). Techniques have been developed to address the need for both better data for models and more accurate in situ large root imaging, including X-ray computed tomography, magnetic resonance imaging, and positron emission tomography (Atkinson et al., 2019; Messina et al., 2021). However, these methods require expensive equipment that is relatively inaccessible for most plant researchers (Topp et al., 2016). Another potential, more accessible route for ex situ measurement of large root systems proposed here is the use of a semiautomated custom lightbox-based system designed for large, intact root systems.

Schematics for root light boxes paired with imaging software have been published as far back as 1980 (Voorhees et al., 1980), and as recently as 2020 (Seethepalli et al., 2020). The basic design has remained relatively stable over time, featuring a camera, light source, and light diffuser (the components of the light box), and often an acrylic or glass box that is placed on the light box and filled with water to keep the roots from matting (Clark et al., 2013; Lobet & Draye, 2013; Voorhees et al., 1980). Many of these camera and light box systems follow the same basic principles as flatbed scanners, taking high contrast, 2-D images of backlit roots. However, digital cameras often use different sensors for image construction and can require corrections for lens distortions or the capture of multiple images rather than a single scan. Some systems incorporate additional features such as rotating stands for gel-grown plants for 3D reconstructions of the roots (Clark et al., 2011; McGrail & McNear, 2021) or clamps to hold roots upright in lieu of floating them in water (Seethepalli et al., 2020).

A key constraint to the adoption of custom light boxes in root phenotyping is lighting non-uniformity. The process of distinguishing roots from the background, or image segmentation, often relies on uniform lighting to differentiate pixel intensities (Yu & Fan, 2017; Zhang et al., 2013). Indeed, scanners are recommended for deconstructive root imaging due to the guaranteed uniformly lit images (Freschet, Pagès, et al., 2020). While flatbed scanners are ubiquitous in root studies, most available scanners offer a

Core Ideas

- Phenotyping of large intact root systems is needed to accelerate crop improvement.
- Advancements in image segmentation have removed the requirement of uniform backlighting.
- Image quality and resolution of our method is equal to that of scanner-based methods.
- Accurate trait data can be extracted from images taken with relatively inexpensive equipment.

23 × 28 cm or 30 × 40 cm field of view, and reported root lengths reach up to 10,000 mm per scan (Adu et al., 2014; Lobet & Draye, 2013; Mohamed et al., 2017). This means that scanning a mature, 400,000 mm maize root system (Han et al., 2020) could take 40 or more individual scans even on the larger end of office scanners. Large-format flatbed scanners, more often used for art preservation, can run upwards of USD$10,000 and are still of limited size. Given the aforementioned interests in large root imaging, refining light box techniques remains relevant and has become more feasible with advances in image processing techniques.

Advances in deep learning and other machine learning approaches have yielded promising results for image segmentation in other research fields. Newer segmentation methods use trainable machine-learning algorithms to classify objects in images, rather than relying on basic thresholding, and have begun to appear in open-source image analysis software. For example, Trainable Weka Segmentation is a tool developed for the segmentation of microscopy images (Arganda-Carreras et al., 2017). It relies on user input to train algorithms to assign pixels to different classes and is readily adaptable for root-background segmentation. RootPainter is another image segmentation tool being developed with roots in mind that similarly uses deep learning and user annotation to distinguish roots from background, including backgrounds as heterogeneous as soil (Smith et al., 2020). While in its current form it requires a higher level of technical experience to set up, Root-Painter shows an encouraging direction for the future of root image analysis.

The aim of this research was to develop a low-cost, large-format 2-D root imaging methodology and provide an example workflow for efficiently going from plant seed to root trait analysis. Here, we describe how this methodology was applied to study maize roots and demonstrate the accuracy of this approach. Maize (*Zea mays* L.) was grown in large mesocosms to the V6 growth stage, at which point the roots were washed free of growth media, staged on a custom-built light box, and imaged using a digital single-lens reflex (DSLR) camera mounted on a computer-controlled motorized rail. A

combination of custom, licensed, and open-source computer programs were then used to process the images. We validated the accuracy of the methodology using model root systems and assessed its throughput by using the platform to determine root traits of a panel of 12 maize hybrids grown to the V6 growth stage.

2 | MATERIALS AND METHODS

2.1 | Experimental design

Twelve commercial maize hybrids spanning 80 yr of breeding (years of release ranging from 1936 to 2014) were grown in five replicate blocks between May and November 2020. The hybrids were part of the Corteva Agriscience Era panel (Duvick et al., 2004), which contains well-studied, commercially successful material from the United States. The plants were grown for s28 d postemergence. The blocks were planted 2 wk apart so that 60 experimental units could be accommodated in 36 greenhouse pots. Greenhouse conditions were set to approximate June growing conditions in Central Kentucky. Supplemental lighting was set to a 14-h light, 10-h dark cycle. Greenhouse exhaust fans were set to vent heat when the temperature exceeded 29.4 °C.

2.2 | Plant propagation

Plants were grown following methods adapted from the Penn State Roots Lab (Penn State Plant Science Roots Lab, 2018). Polyvinyl chloride pipes (PVC, 15 cm diameter, SCH40) were cut to 150 cm length and lined with a heavy duty 10-mm plastic liner (Uline). The bottom ends of the pipes were capped with rounded PVC end caps. A 2.5-cm diameter hole was drilled in the bottom center of each end cap and covered with mesh to prevent loss of growth media and permit drainage and gas exchange. Twelve mesocosms were arranged on a purpose-built wooden rack with 7.5 cm spacing between the mesocosm edges and held in place with rubber straps (Figure 1a).

Mesocosms were filled with a soil-less growth media composed of 50% sand (Quikrete), 40% fine vermiculite (Therm-o-Rock), and 10% perlite by volume. This growth media was selected due to its low-cost, homogeneity, favorable drainage and water retention characteristics, and because it was relatively easy to wash off the roots. For each mesocosm, 33 L of medium were mixed in a concrete mixer with 3.3 L of deionized (DI) water for approximately 2 min until homogeneous. The mesocosms were then filled by hand and periodically pounded against the ground or, when too heavy, struck with a rubber mallet to settle the growth medium. Mesocosms were then secured in the growth rack and watered
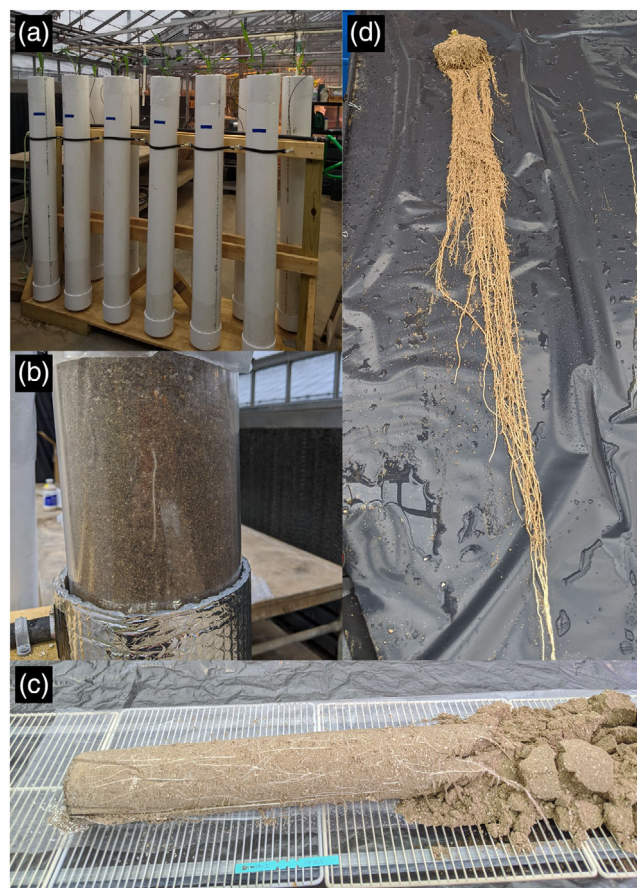

FIGURE 1 Photographs of maize plants growing in the mesocosms (a), root growth being tracked in the clear mesocosm (b), roots on grates for initial cleaning (c), and a root system on the washing table prior to rinsing (d)

to field capacity with 14 L of water, and then equilibrated with an additional 3 L of water twice per day for 10 d. Each mesocosm then received two seeds, 2.54 cm apart at a depth of 2.54 cm, which were then thinned to one plant after emergence. Following planting each mesocosm received 200 mL of full-strength Hoagland Modified Basal Salt Mixture (Phytotech Labs) adjusted to pH 6 with 1 M KOH. After emergence, each mesocosm was watered with 200 mL of solution daily. Plants were grown to the V6 growth stage. Root growth in the PVC cylinders was approximated using a clear acrylic cylinder planted with one of the hybrids as a reference as shown in Figure 1b. This allowed us to time sampling to prevent plants in the mesocosms from becoming root bound.

Plants were prepared for imaging at the V6 growth stage by removing the shoots 1 cm above the aerial nodal roots—at that stage, all plants had only one aerial whorl. Each mesocosm containing the roots and growth medium was then transferred to a table where it was placed horizontally on top of a series of elevated grates (Figure 1c). The endcap was then removed, and the roots and growth media liberated from the PVC pipe by holding one end of the plastic liner while another
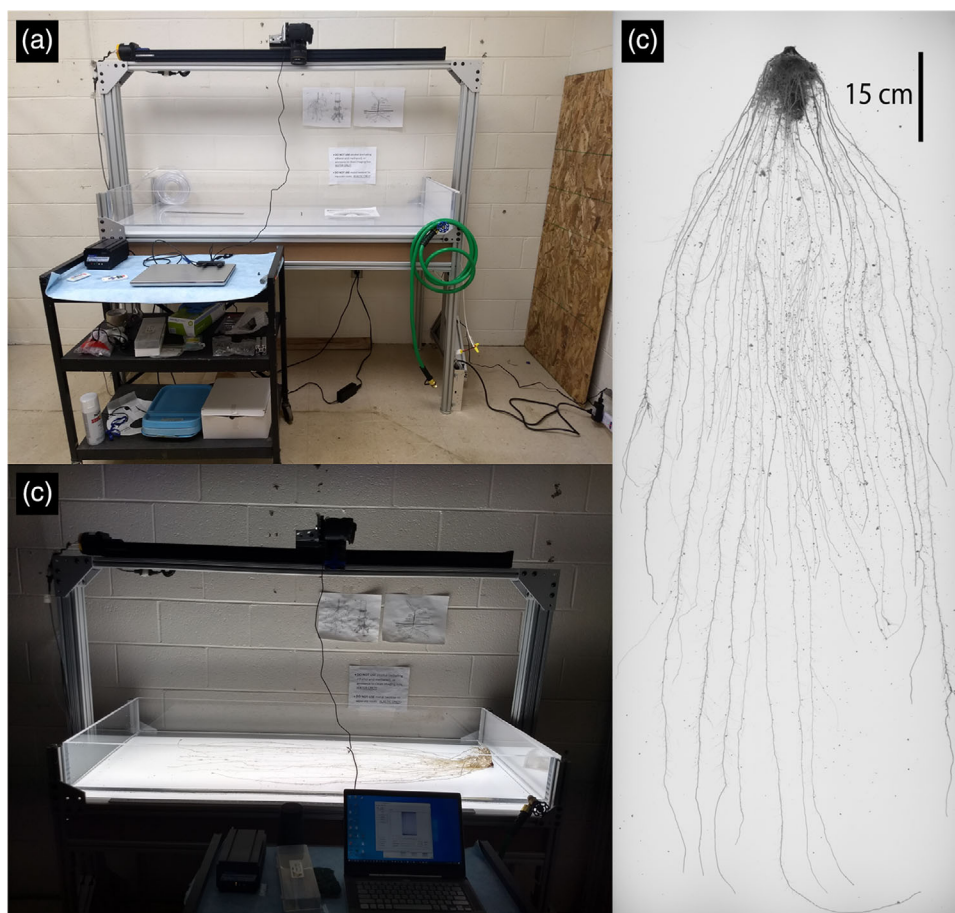
FIGURE 2 The imaging table and the camera rail crossbeam (a), the imaging table illuminated with roots in the acrylic box (b), and an example of a stitched root system image (c)

person pulled from the opposite end of the PVC pipe. A surgical blade was then used to cut the plastic liner longitudinally, after which it was pulled from underneath the growth medium carefully to avoid root breakage. Any growth medium not strongly attached to the roots was pressed through the grates using light pressure or gentle vibration. The root system was then transferred to an adjacent slightly inclined table lined with black plastic and gently washed to remove tightly adhered growth media using the shower setting of a garden hose (Figure 1d). Once washed the intact root systems were submerged in bins of cool DI water and kept refrigerated for up to 3 d until imaged. This process may be adapted for the use of other growth media but may require corresponding changes to the root washing process.

2.3 | Imaging platform

The centerpiece of the imaging platform was a 60 × 150 × 20 cm (W × L × H) clear acrylic box for staging the roots built using 1-cm thick acrylic sheets (Figure 2a). A drain was tapped into the lower side of the box to drain water after imag-

ing. The acrylic box was suspended over a light box built into a table constructed out of aluminum T-slot structural framing (80/20 Inc.). The bottom and sides of the light box were created using cut pieces of gloss white wall paneling (Decorative Panels International) fit into the channel of the T-slot structural framing. Any exposed aluminum framing inside the light box was painted gloss white to increase light reflection and minimize shadowing (Figure 2a). The light box was lit by adhering two 7.31-m low profile dimmable LED tape lights (1549 Lumens each, 3,000 K; Commercial Electric) to the bottom panel of the light box in a sinusoidal pattern lengthwise (each light row ∼ 13 cm apart). A translucent plexiglass panel was used for the top of the light box to provide a diffuse even light, supported on the 80/20 framing under the acrylic box, as shown in Figure 2b. The combination of the frame, light box, and acrylic box is hereafter referred to as the imaging table.

For automated image collection, a motorized 1.5 m rail (Velmex BiSlide, Bloomfield, NY) was suspended over the imaging table by mounting it to a crossbeam structure built using 80/20 (Figure 2a). The rail support was independent of the table to prevent movement of the roots during imaging
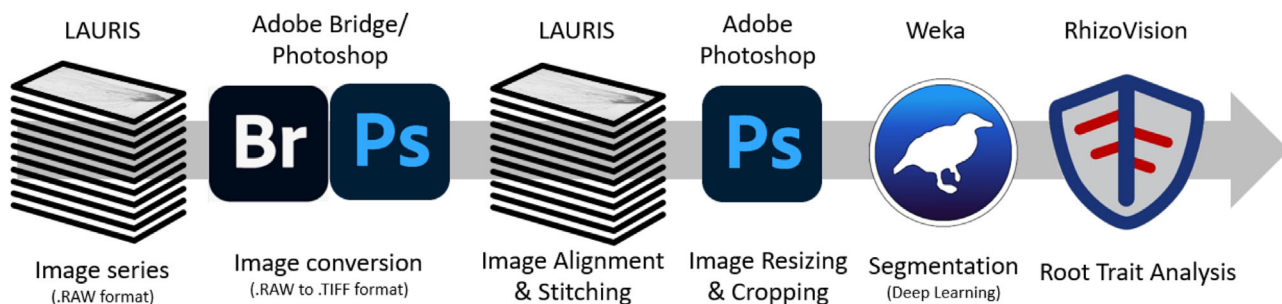
LAURIS	Adobe Bridge/ Photoshop	LAURIS	Adobe Photoshop	Weka	RhizoVision
Image series (.RAW format)	Image conversion (.RAW to .TIFF format)	Image Alignment & Stitching	Image Resizing & Cropping	Segmentation (Deep Learning)	Root Trait Analysis

FIGURE 3 The platforms and programs used for each step of image acquisition and processing for the described method, listed sequentially

that might diminish image quality. A Canon EOS M50 DSLR camera equipped with an EF 28–135 mm f/3.5-5.6 IS USM lens (Canon USA) was attached to the rail carriage using a 3D printed mount to which a quick release Oben QRA-R2 camera mount (B&H Photo) was attached for easy mounting and dismounting of the camera.

2.4 | Image capture and processing

Prior to imaging, the root acrylic box was filled with enough DI water to evenly cover it ($\sim$ 5 mm deep). The roots were then transferred from the buckets to the table and carefully separated using plastic tweezers and spatulas, taking between 15 to 30 min per system, dependent upon size and the degree of root tangling.

Image capture and processing followed the steps listed in Figure 3. Images were taken using the camera attached to the rail. The camera was controlled using LauRootImagingSystem (LAURIS), which provides a graphical user interface (GUI) for the EOS SDK software development kit distributed by Canon. The software offers nearly complete control of the camera over a USB 2.0 connection with a mini-B adapter, with the exceptions of the camera power, zone modes, autofocus, and lens stabilization. The camera was set in the manual zoning mode with autofocus on the lens enabled but stabilization disabled. Turning the camera on and off was performed by hand. Connecting the camera enabled a live feed of the camera's view within LAURIS, as well as manual adjustment of image capture settings and rail movement.

Prior to imaging, all the operations traditionally required of using a DSLR camera in manual mode such as setting the shutter and aperture priority were performed. Focusing of the lens was performed manually in software using the live video with buttons in the GUI that move the lens in small or large increments in either direction. The Canon 50D specifically allows the user to zoom into the image sensor using live view to make these adjustments. In the GUI, this was performed by clicking on a location in the live view display and then enabling or disabling zoom. The zoom lets the user see down

to the pixel level of the sensor, while making lens adjustments along the way. Once the zoom was set by the user, the software did not change the focus during imaging or disable any autofocus functions in the camera.

Sixty-four images were taken per root system by moving the camera a fixed distance along the rail, stopping for a picture, and repeating until the root system was fully captured. This process took approximately 3 min per image set. Images were saved in the raw file format and were then converted to greyscale Tag Image File Format (TIFF) using the Adobe Photoshop image processor tool in Adobe Bridge (Adobe Inc.) using the following default settings: the profile was set to Adobe monochrome; the white balance was as shot; the temperature was set to 5,950 K; and the tint was set to +20. All other basic adjustments were left at 0.

To correct for the barrel distortion that occurs with all camera lenses and to combine all captured frames into a single image, we implemented the CALTag calibration procedure (Atcheson et al., 2010) using LAURIS. We used a CALTag grid consisting of 7.35 × 7.25 cm squares that were printed to a size matching the dimensions of the imaging table and then imaged as described previously. The CALTag procedure was based on the checkerboard calibration commonly associated with OpenCV and MATLAB computer vision libraries but also included a separate checkerboard, similar to a QR code, inside each square of the original board that fills the central 50% area of the square. The squares of these internal checkerboards were assigned a black or white value according to a 16-bit binary code unique to its location. By having this unique code, the checkerboard could be accurately detected even when portions of the board were occluded from or outside the camera's field of view.

The procedure for detecting the CALTag pattern is documented in Atcheson et al. (2010), who have made the MATLAB source code available for public use. The C++ implementation used in this study is also available on github by the author, Daniel Lau (github.com/drhalftone). Briefly, the process involves applying an adaptive thresholding operation that converts a photograph of the calibration target into

a binary image with the edges of the squares found using OpenCV's edge detection filters and then fitting a quadrilateral to the resulting contours. Squares that were determined to be within the expected range in terms of area were then further processed by looking for saddle points. A random sample and consensus algorithm (RANSAC) was then used to identify the saddle points forming a 2-D grid. This grid fitting was improved by incorporating a radial distortion lens model. From the resulting grid, spatial coordinates for the 16-bit binary codes were calculated and the bits decoded. Another RANSAC process was performed based on these codes such that unique global XY coordinates were assigned to the saddle points. This included interpolating and extrapolating XY coordinates for occluded saddle points. Once each saddle point had a unique XY coordinate, a mapping of camera rows and columns to global XY coordinates was derived such that each pixel in the captured image had a unique XY location. As we were using a CALTag checkerboard that covered the entire surface of the imaging table, we could assign a unique XY coordinate to each pixel of every photograph, forming a stitched image.

The stitching of images was performed using two sets of images. The first set of images consisted of 64 images of the printed CALTag grid while the second set of images corresponded to the 64 images of a root system. Since both sets of images were taken in virtually the same location along the rail, the XY coordinates of corresponding images are assumed identical. As such, we assigned to each root image the corresponding XY coordinates from the CALTag images. The stitched image was then formed by creating an image buffer where each pixel of the buffer has a predefined XY coordinate on the table. For each pixel in the buffer, we mapped its XY coordinate to the XY coordinates in the series of root images. There were typically multiple images that had a pixel with the same XY coordinate, with a degree of overlap between sequential images of approximately 95%. Our stitching process chose the pixel from the images that was closest to the center of a particular image's field of view so that the selected pixel corresponded to the camera position looking straight down on the roots. Since the XY coordinates were defined by the CALTag images, this process of searching root images for pixels was performed by a look-up table process where the look-up table or mapping was calculated when the CALTag images were processed. Note that changing the soft limits of the image collection or even the number of images forming a stitched image required redoing the collection and processing of the CALTag checkerboard.

Because of the high level of matting of the roots near the crown (Figure 2c), the top 15 cm of the root systems were processed separately to better capture the crown root traits. After imaging the whole root system, the crowns were physically removed, deconstructed into individual nodal roots, and imaged using a separate platform consisting of a stationary

camera over a smaller (46 × 61 cm) acrylic box for staging roots placed on top of a light box (Gagne Porta-Trace). This allowed crown imaging and whole system imaging to be worked on simultaneously. Stitched images of the whole systems were cropped into six depth increments for analysis and exported from Photoshop as 16-bit uncompressed TIFFs. For the purposes of this study, the average values for the 15–150 cm root depths are presented.

Following alignment, calibration, stitching, and cropping, the images were segmented using the Trainable Weka Segmentation plugin built into FIJI (Arganda-Carreras et al., 2017; Schindelin et al., 2012). The plugin uses user-generated training data to build a machine-learning algorithm for image segmentation. The segmentation model was trained with two classes: root and background. Samples were added to each class until the model performed well across multiple test images. Fifteen training examples were used for each class. In addition to sample number, sample quality is important. Selected samples covered the range of pixel values for both classes, and particular attention was given to the transition between root edge and background. Due to image size constraints of the plugin, cropped sections of images with variable backlighting were used. The most accurate segmentation of the background and roots was obtained with the default training features, which include Gaussian blur, Hessian matrix, Sobel filter, differences of Gaussians, and membrane projections. The classifier used was the default FastRandomForester classifier, and it was initialized with 200 trees and two random features per node. Due to random access memory (RAM) constraints with large images (ours ranged from 4,800 × 1,225 to 4,800 × 2,450 pixels, depending on the depth section), the built-in batch processing function performed poorly. Instead, an ImageJ Beanshell script was used that subdivides each image into a grid of tiles which are processed individually to preserve RAM ("Scripting the Trainable Weka Segmentation," 2021). The script output stacks of probability maps for each class as 32-bit TIFFs. Macros were written and used to separate the root probability maps from the stacks and threshold them in ImageJ using default settings. Because of root analysis software constraints, the images were converted back to 16-bit TIFFs following the thresholding processing. Figure 4 shows an example of a root image at each stage of preprocessing. Processed images were checked to ensure that background sections were correctly thresholded following segmentation. Note that simpler thresholding methods using only ImageJ were attempted and proved inadequate. RootPainter was mentioned previously as another machine learning-based image segmentation tool, but we found that it requires a significant amount of dedicated RAM as well as a dedicated server. Thus, while it was built for root system segmentation, the hardware requirements presented a constraint to its use for our application.
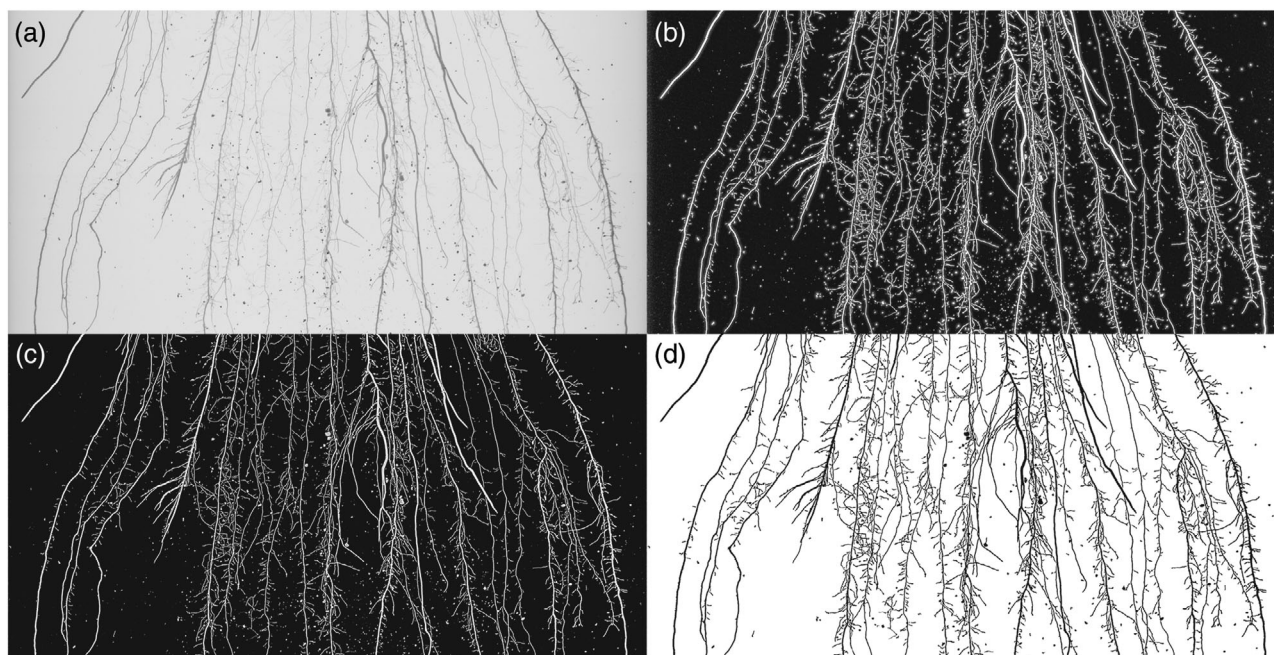
FIGURE 4 A cropped section of a root image at various stages of preprocessing, including the initial grayscale image (a), the probability map generated by Weka Trainable Segmentation (b), the thresholded image generated in FIJI (c), and the final segmented image produced by RhizoVision Explorer (d)

2.5 | Root trait measurements

A test set of 10 thresholded images were individually loaded into Rhizovision Explorer (Seethepalli & York, 2020) to determine the settings that minimized alterations to the input images and limited erroneous root detection. The "filter noisy background components" option was used to remove residual perlite and vermiculite from the images. The settings were saved and then applied to each block of images via the batch processing feature. One block was excluded from analysis due to imaging errors from an earlier iteration of the imaging table. The mean root diameter, total root length, total root volume, total root surface area, and length of six different root diameter classes were collected for each image to assess the extractability of the root morphological trait data.

2.6 | Measurement validation

We used model root systems to evaluate the accuracy of root trait measurements taken from images captured with the imaging table as well as those captured with a scanner. Seven artificial root models were constructed out of varying lengths of nylon monofilament of three different diameters: 0.3, 0.7, and 1.2 mm. These diameters were chosen to reflect the range of root diameters in maize roots (Costa et al., 2002, 2011). The lengths of each diameter for each model were measured using a ruler, and the diameters were confirmed with a

digital micrometer. Ground-truth surface area and volume of the models were calculated under the assumption that the filaments were perfect cylinders. Ground-truth values for each model are given in Supplemental Table S1. The 0.3-, 0.7-, and 1.2-mm filaments were colored with pink, tan, and brown Sharpie permanent markers (Newell Brands), respectively, to mimic the variable opacity of actual roots (Figure 5). The traits assessed were total root length, average root diameter, the length of each size class, total surface area, and total volume.

We imaged the model root systems with the imaging table and processed the images following the previously described protocol. We then analyzed the images in batches with RhizoVision Explorer using the following settings: broken roots; image thresholding level of 255; "filter noisy background components" set to true; "maximum noisy component size" set to 0.5 mm^2; and "root pruning threshold" set to five pixels.

To collect scanned images, we used an Epson Perfection V700 Photo (Epson America, Los Alamitos, California) with a transparency unit. The scan resolution was 300 dpi and images were saved as both 16-bit and 8-bit grayscale TIFFs. A scan resolution of 600 dpi was also evaluated but performed the same as 300 dpi for the model root systems. We then batch analyzed the images with RhizoVision Explorer using the same settings as above apart from the image thresholding level being set at 215, as the scans had not already been thresholded.

FIGURE 5 An example of a monofilament root model photographed against a white cloth background. Pink filament has a diameter of 0.3 mm, tan filament has a diameter of 0.7 mm, and the dark brown filament has a diameter of 1.2 mm. Plastic chip is 1 cm × 1 cm
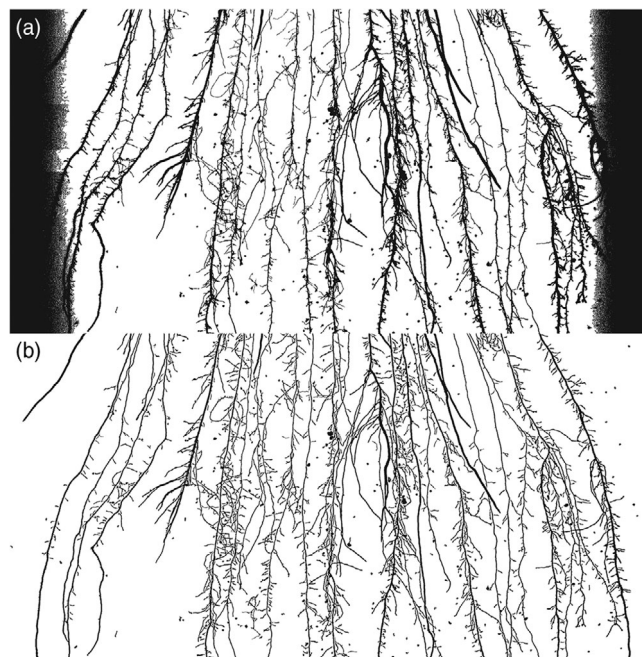

FIGURE 6 A cropped root image segmented in RhizoVision Explorer without preprocessing (a) and following segmentation using Weka Trainable Segmentation and thresholding with FIJI (b). The black specks are residual perlite and vermiculite particles from the growth media, which were later filtered out using functions within RhizoVision Explorer

2.7 | Statistics

Linear regression was used to obtain the coefficient of determination (R^2) between the ground-truth measurements and the estimated measurements using the two imaging platforms. To assess error associated with the imaging platforms, the root mean square error (RMSE) and mean bias error (MBE) were calculated for each measured trait. RMSE is the standard deviation of the residuals, while MBE is the average amount by which the ground-truth values are greater than the estimated values (i.e., positive values indicate underestimation and negative values indicate overestimation). The normalized RMSE (nRMSE) was also calculated by dividing the RMSE for each trait by the mean for that trait, allowing for a comparison of accuracy across all traits. All statistical analyses were performed in R version 1.4.1106 (R Core Team, 2021). The packages "lemon" (Edwards et al., 2020), "ggplot2" (Wickham, 2016), "ggpubr" (Kassambara, 2020), and "ggpmisc" (Aphalo, 2021) were used for data visualization. The package "Metrics" (Hammer & Frasco, 2018) was used to calculate the model performance metrics.

3 | RESULTS

3.1 | Root trait measurements

Image stitching took approximately 20 min per root system, while image segmentation and analysis took approximately 13 min per root system. Out of the set of 330 maize root images, no processed images exhibited the dark edge or diameter overestimation issues that arose when thresholding unprocessed images (Figure 6a). While no images showed the background incorrectly segmented as roots, sections of the finer roots near branching points were sometimes classified as background, as seen in Figure 6b. Using the known true size of the images and the pixel dimensions, the images captured with the imaging table were calculated to have a resolution of 207 dpi.

Our root phenotyping platform captured average diameter, surface area, total volume, total length, and length of six diameter classes for maize root systems spanning a wide range of measured values (Figure 7).

3.2 | Trait Measurement Validation

The analysis of scanned images was less accurate for 16-bit scans than for 8-bit scans (Supplemental Table S2, Supplemental Figure S1), and as such the 8-bit scans were used for comparison to the imaging table results. Estimated values
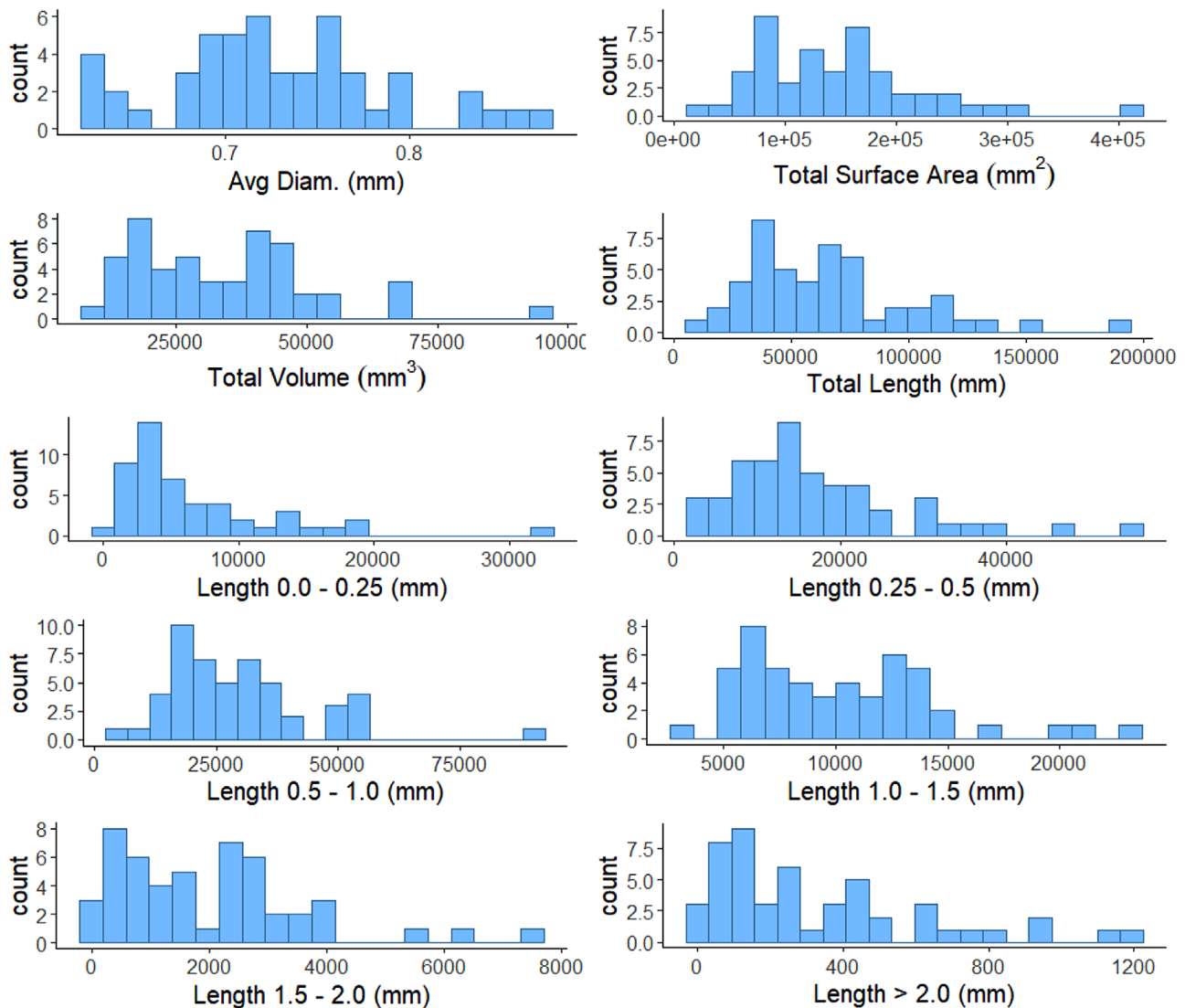
FIGURE 7 Histograms showing the frequency of root traits values for root systems of the maize panel (*n* = 50). The counts are for the total values for the 15–150 cm depths of each root system

were well correlated with ground-truth values for all traits and both platforms, with R^2 values ranging from 0.90 to 1.0, and averaging 0.96 for both platforms (Figure 8). RMSE values indicated that the table platform was more accurate than the scanner platform for traits related to root diameter, including average diameter, the length in each size class, surface area, and volume. The scanner was more accurate for total length estimates, though the imaging table was slightly more accurate than the scanner for the smallest and largest root size class lengths. Normalized root mean square error values were at or under 20% for all seven measured traits for both platforms (Table 1) and indicate that the scanner most accurately estimated total length, while the imaging table most accurately estimated average diameter. Mean bias error values were negative for all traits for both platforms except for the length of the 0.0–0.5 mm size class for the scanner, indicating a general overestimation of root trait measurements (Table 1).

4 | DISCUSSION

The aim of this project was to develop a relatively low-cost, large-format 2-D root imaging platform and image analysis methodology and provide an example procedure for efficiently going from plant seed to root trait analysis. In total, the materials for the imaging table cost approximately $4,000, with a breakdown of $1,500 for the 80/20 and light box materials, $400 for the acrylic box for staging roots, $500 for the camera, and $1,000 for the automated rail. Note that the rail was in used condition, and the controllers were provided free of cost. The cost could be lowered with the use of less expensive framing materials, cameras, and rails. By comparison, the largest scanner for that cost is 30 × 40 cm, before factoring in the cost of an acrylic box.

TABLE 1 Accuracy metrics for the analysis of the monofilament root models using the imaging table and scanner platforms

Traits	Platform	RMSE	nRMSE (%)	Mean bias error	Coefficient of determination	*p*-value
Average diameter (mm)	Scanner	0.08	11.11	−0.08	0.90	.001
	Table	0.03	4.25	−0.02	0.90	.001
Length 0.0–0.5 mm (mm)	Scanner	33.50	16.53	25.74	0.95	<.001
	Table	24.94	10.50	−9.32	0.96	<.001
Length 0.5–1.0 mm (mm)	Scanner	17.52	7.31	−9.93	0.97	<.001
	Table	23.33	9.76	−9.43	0.94	<.001
Length > 1.0 mm (mm)	Scanner	23.85	12.82	−19.17	0.99	<.001
	Table	13.19	7.37	−12.00	1.00	<.001
Total length (mm)	Scanner	21.08	3.36	−3.37	0.98	<.001
	Table	39.37	6.01	−30.74	0.97	<.001
Total surface Area (mm^2)	Scanner	175.20	11.62	−154.75	0.99	<.001
	Table	136.93	9.36	−110.06	0.96	<.001
Total volume (mm^3)	Scanner	75.15	20.78	−68.44	0.98	<.001
	Table	32.21	10.08	−26.41	0.97	<.001

Note. RMSE, root mean square error of mean; nRMSE, normalized root mean square error.

4.1 | Advantages of the large root system imaging platform

Using the imaging table, we were able to capture a wide distribution of maize root traits. Our imaging table produced root measurements that were in good agreement with ground-truth values, yielding slightly more accurate results overall compared with scanned images. The imaging table enabled us to measure total root lengths up to 200,000 mm across the five depth increments of each root system, and as low as 50 mm in a single image. For comparison, total root lengths reported in scanner-based studies typically range between 10 and 10,000 mm (Adu et al., 2014; Lobet & Draye, 2013). Although in this study we focused on the 15–150 cm depths captured on the imaging table, the same methodology could be applied to the deconstructed 0–15 cm roots that were imaged separately. In addition to the traits measured, this system allows us to easily capture the depth distribution of root length using the cumulative length at multiple depths (Fan et al., 2016), which is of increasing interest for both deep soil carbon and crop performance (Lynch, 2013; Lynch & Wojciechowski, 2015; Nuccio, 2021). While depth distribution can be captured using a smaller scanner, this system offers greater flexibility and lower risk of error by not requiring that roots be subdivided into several subsamples within preselected depth ranges. It should be noted that this system and 2-D systems in general are not suitable for the collection of crown root angle dependent traits such as maximum width or convex hull volume. However, as noted in Rangarajan and Lynch (2021), 2-D platforms do provide accurate information on parameters such as number, length, and diameter of roots,

lateral root branching density, and others that provide accurate estimates of overall root system morphology and architecture and possible functional attributes.

Our system and process expand the ability of researchers to study roots of older and larger plants by removing the need to fully dissect the root system to fit the smaller dimensions of commercially available scanners. While the root staging time is longer than for a small scanner, each system only has to be prepared for imaging once rather than across several subsamples. With this system we were able to capture up to 200,000 mm of length in one run, but in other work on loose roots we found that the maximum length we could stage within a scan on an Epson Perfection V700 Photo (23 × 28 cm) was around 4,000 mm. Assuming a relatively quick time of 5 min per scan (changing the water, staging the roots, taking the scan), processing a 200,000 mm system could take at minimum 4 h. With a maximum of around 30 min for staging and imaging, the proposed method results in substantial time savings when working with large root systems. This also reduces the time that roots need to be kept fresh, preventing decomposition and loss of structural integrity, and eliminating the need for alcohol or other preservatives that could limit any desired chemical analysis on the tissues after imaging.

4.2 | Accuracy of the large root system imaging platform as compared to a scanner approach

Each step of root image processing can introduce error or limit how comparable results will be across methods. While it
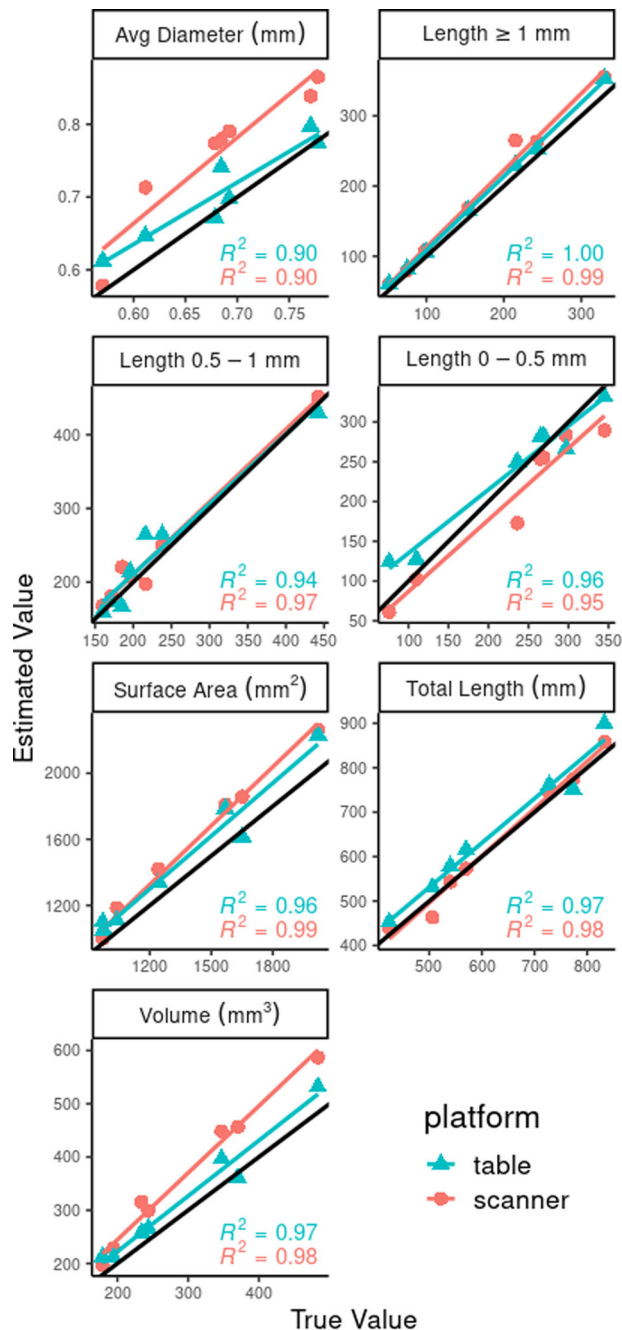
FIGURE 8 Linear regression lines and coefficients of determination for each trait measured for the 8-bit scans and imaging table photographs of the model root systems. The black line is a 1:1 line. Points over the black line indicate overestimation; points under the line indicate underestimation

and more consistent accuracy. This suggests that, with a well-trained segmentation model, the imaging table method is a viable option.

The relatively high inaccuracy for the scanned images appears to stem from the overestimation of diameter. As volume and surface area calculations are both based on diameter estimates, it follows that an overestimation of diameter will lead to an overestimation of both of those traits. Similarly, the amount of root length in each size class will be incorrectly estimated, as some roots from the 0.0–0.5 and 0.5–1.0 mm classes would be shifted to the 0.5–1.0 and >1.0 mm classes, respectively. This helps explain why, while the total length estimate for the scanned images is the most accurate estimation across traits and platforms, the scanned images had higher error for the smallest and largest size classes.

That the diameter in the scanned images was less accurately estimated than in the imaging table images and that greater bit depth exacerbated this (Table S2, Figure S1) was unexpected, as scanned images have previously been demonstrated to give highly accurate diameter estimates (Seethepalli et al., 2021). To build on the comparison between the imaging table and flatbed scanners and assess whether this overestimation is a consistent finding, testing a wider range of filament diameters across multiple scanners at both 300 and 600 dpi would help ensure that the differences seen here are not due to hardware limitations, as the quality of the optics themselves can make a significant difference in analysis (Freschet, Pagès, et al., 2020). To the authors' knowledge, no formal investigation has been made into bit depth affecting diameter accuracy, and thus that finding also merits further testing. While the results here suggest consistent overestimation of diameter for scans within the range tested and the 207 dpi resolution of the table images did not appear to limit the accuracy of trait analysis, root hairs were not well-captured in the images of true roots. Thus, at the moment, high-resolution scanner-based approaches likely remain more appropriate for that application. The use of higher quality sensors and lenses, as well as the use of a two-dimensional rail structure, could increase resolution well beyond the limits of available scanners but may also significantly increase the cost of the system.

Using our image processing method, it was possible to accurately segment the images as compared to the pixel intensity method built into many root analysis programs. The segmented maize root images and the results from the model root system indicate that even the faint, thinnest roots (at least as thin as 0.3 mm in diameter) were detectable and reasonably well estimated using this approach. As the other solution to poor segmentation of fine roots is to stain them (Freschet, Pagès, et al., 2020), machine learning-based segmentation may be preferable when also performing chemical analyses of the root samples.

cannot account for all methodological differences, comparing the results using different imaging platforms to ground-truth values does give some sense of both how accurate the results are and how comparable they are to methods currently in use. In this case, the estimates for the images of the root models taken with the flatbed scanner and the imaging table were similarly accurate, with the imaging table having an overall higher

4.3 | Limitations of the large root system imaging platform

The major limitations of the proposed method are that it requires using several different software platforms and that machine-learning based image segmentation is memory intensive. Since the data were collected for this manuscript, the second step of image analysis (Figure 3) has been incorporated into LAURIS, replacing the use of Adobe products. The updated version is available at https://github.com/drhalftone/LAURootImagingSystem. Combining image capturing, alignment, calibration, and stitching within a single platform will reduce acquisition and processing time in future experiments. There are also limitations with some of the other specific programs used. The Weka segmentation plugin was designed for differentiating cell types in microscopy images, and, as such, it has a limited capacity to handle large image file sizes, resulting in a slow training and segmentation process. Given this limitation, cropping images of the complete stitched root system will continue to be necessary regardless of the aims of the project, until a purpose-built program is developed. Planned improvements to LAURIS include continuing to streamline the method by combining the processing steps listed in Figure 3 within a single, open-source program, as well as the elimination of image stitching through modifications to the camera controls. Through the integration of tools such as Intel oneAPI and OpenCV, the software can be further optimized for processing images on low-power computers.

4.4 | Growth media considerations

Our central goal in phenotyping was to compare the potentials of different lines under the same conditions. As such, we used a mesocosm system that allowed the roots to grow unconstrained in terms of vertical space and resources. The combination of sand, perlite, and vermiculite that we adopted from the Penn State greenhouse methods resulted in a realistic bulk density and adequate water and nutrient retention. The mixture was low-cost, homogeneous, easy to acquire, relatively light-weight, well-drained, and easy to remove from roots. One challenge with this growth medium was that the perlite and vermiculite could not be completely removed due to the fragility of the roots and the tendency of the roots to grow through these particles. This contamination was addressed using the noise filtering function of RhizoVision Explorer. Nevertheless, this overall process is certainly not limited to the growth medium that we used. Other studies have used gels, natural soils, or materials such as calcined clay (Numajiri et al., 2021; Paez-Garcia et al., 2015), but each comes with its own tradeoffs that must be weighed for any given application. While a sandy soil could potentially be suitable for phenotyping work, finer textured soils would require much more care and labor to leave the root systems intact while washing. In addition, as one crucial aspect of phenotyping is maintaining consistent conditions for the plants grown, the inherent heterogeneity of natural soils poses a significant challenge for sourcing and repeatability when working in greenhouses. While our approach is not directly translatable to field phenotyping results, it does give a sense of the potentials of the different lines that can inform selections for field trials.

5 | CONCLUSIONS

Large root imaging and analysis has been limited by the cost of suitable equipment, the size capacity of more widely available equipment, and the need for uniform lighting in root images. To address this, we built a custom imaging table and developed an image processing method suitable for large root images with non-uniform lighting. Trait measurements using this method have similar accuracy to those from the standard scanner method, indicating that lighting is no longer a significant barrier to 2-D root phenotyping. With the added benefits of time savings and greater ease of analyzing traits by depth, this work will open up more opportunities for large root analysis, while maintaining high accuracy and low cost.

AUTHOR CONTRIBUTIONS
Brian Rinehart: Conceptualization; Data curation; Formal analysis; Investigation; Methodology; Visualization; Writing – original draft; Writing-review & editing. Hanna Poffenbarger: Conceptualization; Funding acquisition; Supervision; Writing – review & editing. Daniel Lau: Methodology; Software; Writing – original draft. Dave McNear: Conceptualization, Funding acquisition, Methodology, Resources, Supervision, Writing-original draft, Writing-review & editing.

CONFLICT OF INTEREST
The authors declare no conflict of interest.

ORCID

Brian Rinehart https://orcid.org/0000-0002-3990-2365
Hanna Poffenbarger https://orcid.org/0000-0002-7715-373X
Daniel Lau https://orcid.org/0000-0003-1377-4622
Dave McNear https://orcid.org/0000-0003-4828-8763

REFERENCES

Adu, M. O., Chatot, A., Wiesel, L., Bennett, M. J., Broadley, M. R., White, P. J., & Dupuy, L. X. (2014). A scanner system for high-resolution quantification of variation in root growth dynamics of Brassica rapa genotypes. *Journal of Experimental Botany*, 65(8), 2039–2048. https://doi.org/10.1093/jxb/eru048

Aphalo, P. J. (2021). *ggpmisc: Miscellaneous Extensions to "ggplot2"* (0.4.0). https://CRAN.R-project.org/package=ggpmisc

Arganda-Carreras, I., Kaynig, V., Rueden, C., Eliceiri, K. W., Schindelin, J., Cardona, A., & Sebastian Seung, H. (2017). Trainable Weka Segmentation: A machine learning tool for microscopy pixel classification. *Bioinformatics*, 33(15), 2424–2426. https://doi.org/10.1093/bioinformatics/btx180

Atcheson, B., Heide, F., & Heidrich, W. (2010). CALTag: High precision fiducial markers for camera calibration. In R. Koch, A. Kolb, & C. Rezk-Salama (Eds.), Vision, modeling & visualization (pp. 41–48). The Eurographics Association. https://doi.org/10.2312/PE/VMV/VMV10/041-048

Atkinson, J. A., Pound, M. P., Bennett, M. J., & Wells, D. M. (2019). Uncovering the hidden half of plants using new advances in root phenotyping. *Current Opinion in Biotechnology*, 55, 1–8. https://doi.org/10.1016/j.copbio.2018.06.002

Clark, R. T., Famoso, A. N., Zhao, K., Shaff, J. E., Craft, E. J., Bustamante, C. D., Mccouch, S. R., Aneshansley, D. J., & Kochian, L. V. (2013). High-throughput two-dimensional root system phenotyping platform facilitates genetic analysis of root growth and development. *Plant, Cell & Environment*, 36(2), 454–466. https://doi.org/10.1111/j.1365-3040.2012.02587.x

Clark, R. T., MacCurdy, R. B., Jung, J. K., Shaff, J. E., McCouch, S. R., Aneshansley, D. J., & Kochian, L. V. (2011). Three-dimensional root phenotyping with a novel imaging and software platform. *Plant Physiology*, 156(2), 455–465. https://doi.org/10.1104/pp.110.169102

Comas, L., Becker, S., Cruz, V. M. V., Byrne, P. F., & Dierig, D. A. (2013). Root traits contributing to plant productivity under drought. *Frontiers in Plant Science*, 4, https://doi.org/10.3389/fpls.2013.00442

Costa, C., Dwyer, L., Dutilleul, P., Foroutan-pour, K., Liu, A., Hamel, C., & Smith, D. (2011). Morphology and fractal dimension of root systems of maize hybrids bearing the leafy trait. *Canadian Journal of Botany*, 81, 706–713. https://doi.org/10.1139/b03-058

Costa, C., Dwyer, L., Zhou, X., Dutilleul, P., Hamel, C., Reid, L., & Smith, D. (2002). Root morphology of contrasting maize genotypes. *Agronomy Journal*, 94, 96–101. https://doi.org/10.2134/agronj2002.0096

Downie, H. F., Adu, M. O., Schmidt, S., Otten, W., Dupuy, L. X., White, P. J., & Valentine, T. A. (2015). Challenges and opportunities for quantifying roots and rhizosphere interactions through imaging and image analysis. *Plant, Cell & Environment*, 38(7), 1213–1232. https://doi.org/10.1111/pce.12448

Duvick, D. N., Smith, J. S. C., & Cooper, M. (2004). Long-term selection in a commercial hybrid maize breeding program. *Plant Breeding Reviews*, 24(2), 109–152.

Edwards, S. M., Auguie, B., Jackman, S., Wickham, H., & Chang, W. (2020). *lemon: Freshing up your "ggplot2" Plots* (0.4.5). https://CRAN.R-project.org/package=lemon

Fan, J., McConkey, B., Wang, H., & Janzen, H. (2016). Root distribution by depth for temperate agricultural crops. *Field Crops Research*, 189, 68–74. https://doi.org/10.1016/j.fcr.2016.02.013

Fletcher, D. M. M., Ruiz, S., Dias, T., Petroselli, C., & Roose, T. (2020). Linking root structure to functionality: The impact of root system architecture on citrate-enhanced phosphate uptake. *New Phytologist*, 227(2), 376–391. https://doi.org/10.1111/nph.16554

Freschet, G. T., Pagès, L. L., Iversen, C., Comas, L. H., Rewald, B., Roumet, C., Klimešová, J., Zadworny, M., Poorter, H., Postma, J. A., Adams, T. S., Bagniewska-Zadworna, A., Bengough, A. G., Blancaflor, E. B., Brunner, I., Cornelissen, J. H. C., Garnier, E., Gessler, A., Hobbie, S. E., … Mccormack, M. L. (2020). *A starting guide to root ecology: Strengthening ecological concepts and standardizing root classification, sampling, processing and trait measurements.* https://hal.archives-ouvertes.fr/hal-02918834

Freschet, G. T., Roumet, C., Comas, L. H., Weemstra, M., Bengough, A. G., Rewald, B., Bardgett, R. D., De Deyn, G. B., Johnson, D., Klimešová, J., Lukac, M., McCormack, M. L., Meier, I. C., Pagès, L., Poorter, H., Prieto, I., Wurzburger, N., Zadworny, M., Bagniewska-Zadworna, A., … Stokes, A. (2020). Root traits as drivers of plant and ecosystem functioning: Current understanding, pitfalls and future research needs. *New Phytologist*, 232(3), 1123–1158.

Guo, H., & York, L. M. (2019). Maize with fewer nodal roots allocates mass to more lateral and deep roots that improve nitrogen uptake and shoot growth. *Journal of Experimental Botany*, 70(19), 5299–5309. https://doi.org/10.1093/jxb/erz258

Hammer, B., & Frasco, M. (2018). *Metrics: Evaluation metrics for machine learning* (0.1.4). https://CRAN.R-project.org/package=Metrics

Han, Y., Zhang, X., & Ma, X. (2020). Fine root length of maize decreases in response to elevated CO2 levels in soil. *Applied Sciences*, 10(3), 968. https://doi.org/10.3390/app10030968

Kassambara, A. (2020). *ggpubr: "ggplot2" based publication ready plots* (0.4.0). https://CRAN.R-project.org/package=ggpubr

Lobet, G., & Draye, X. (2013). Novel scanning procedure enabling the vectorization of entire rhizotron-grown root systems. *Plant Methods*, 9(1), 1. https://doi.org/10.1186/1746-4811-9-1

Lynch, J. P. (2013). Steep, cheap and deep: An ideotype to optimize water and N acquisition by maize root systems. *Annals of Botany*, 112(2), 347–357. https://doi.org/10.1093/aob/mcs293

Lynch, J. P., & Wojciechowski, T. (2015). Opportunities and challenges in the subsoil: Pathways to deeper rooted crops. *Journal of Experimental Botany*, 66(8), 2199–2210. https://doi.org/10.1093/jxb/eru508

Man, J., Tang, B., Xing, W., Wang, Y., Zhao, X., & Bai, Y. (2020). Root litter diversity and functional identity regulate soil carbon and nitrogen cycling in a typical steppe. *Soil Biology and Biochemistry*, 141, 107688. https://doi.org/10.1016/j.soilbio.2019.107688

McCormack, M. L., Guo, D., Iversen, C. M., Chen, W., Eissenstat, D. M., Fernandez, C. W., Li, L., Ma, C., Ma, Z., Poorter, H., Reich, P. B., Zadworny, M., & Zanne, A. (2017). Building a better foundation: Improving root-trait measurements to understand and model plant and ecosystem processes. *New Phytologist*, 215(1), 27–37. https://doi.org/10.1111/nph.14459@10.1111/(ISSN)1469-8137.ROOT_TRAITS

McGrail, R. K., Van Sanford, D. A., & McNear, D. H. (2020). Trait-based root phenotyping as a necessary tool for crop selection

and improvement. *Agronomy*, *10*(9), 1328. https://doi.org/10.3390/agronomy10091328

McGrail, R. K., & McNear, D. H. (2021). Two centuries of breeding has altered root system architecture of winter wheat. *Rhizosphere*, *19*, 100411. https://doi.org/10.1016/j.rhisph.2021.100411

Messina, C. D., McDonald, H., Poffenbarger, R., Clark, A., Salinas, Y., Fang, C., Gho, T., Tang, G., Graham, G., & Cooper, M. (2021). Reproductive resilience but not root architecture underpins yield improvement under drought in maize (*Zea mays* L.). *Journal of Experimental Botany*, *72*(14), 5235–5245.

Mohamed, A., Monnier, Y., Mao, Z., Lobet, G., Maeght, J.-L., Ramel, M., & Stokes, A. (2017). An evaluation of inexpensive methods for root image acquisition when using rhizotrons. *Plant Methods*, *13*(1), 11. https://doi.org/10.1186/s13007-017-0160-z

Moore, J. A. M., Sulman, B. N., Mayes, M. A., Patterson, C. M., & Classen, A. T. (2020). Plant roots stimulate the decomposition of complex, but not simple, soil carbon. *Functional Ecology*, *34*(4), 899–910. https://doi.org/10.1111/1365-2435.13510

Nuccio, E. (2021). *Deeply rooted: Evaluating plant rooting depth as a means for enhanced soil carbon sequestration* (LLNL-TR-828789). U.S. Department of Energy Office of Scientific and Technical Information. https://doi.org/10.2172/1829022

Numajiri, Y., Yoshino, K., Teramoto, S., Hayashi, A., Nishijima, R., Tanaka, T., Hayashi, T., Kawakatsu, T., Tanabata, T., & Uga, Y. (2021). iPOTs: Internet of Things-based pot system controlling optional treatment of soil water condition for plant phenotyping under drought stress. *The Plant Journal*, *107*(5), 1569–1580. https://doi.org/10.1111/tpj.15400

Paez-Garcia, A., Motes, C., Scheible, W.-R., Chen, R., Blancaflor, E., & Monteros, M. (2015). Root traits and phenotyping strategies for plant improvement. *Plants*, *4*(2), 334–355. https://doi.org/10.3390/plants4020334

Penn State Plant Science Roots Lab. (2018, May 27.) *Mesocosms for root evaluation*. Penn State Plant Science Roots Lab. https://plantscience.psu.edu/research/labs/roots/methods/rootbox-greenhouse-methods/cylinders-for-root-evaluation

Phillips, R. P., Finzi, A. C., & Bernhardt, E. S. (2011). Enhanced root exudation induces microbial feedbacks to N cycling in a pine forest under long-term CO2 fumigation. *Ecology Letters*, *14*(2), 187–194. https://doi.org/10.1111/j.1461-0248.2010.01570.x

Poirier, V., Roumet, C., & Munson, A. D. (2018). The root of the matter: Linking root traits and soil organic matter stabilization processes. *Soil Biology and Biochemistry*, *120*, 246–259. https://doi.org/10.1016/j.soilbio.2018.02.016

R Core Team. (2021). *R: A language and environment for statistical computing*. R Foundation for Statistical Computing. https://www.R-project.org/

Rangarajan, H., & Lynch, J. P. (2021). A comparative analysis of quantitative metrics of root architecture. *Plant Phenomics*, *2021*, 6953197. https://doi.org/10.34133/2021/6953197

Reynolds, M., Atkin, O. K., Bennett, M., Cooper, M., Dodd, I. C., Foulkes, M. J., Frohberg, C., Hammer, G., Henderson, I. R., Huang, B., Korzun, V., McCouch, S. R., Messina, C. D., Pogson, B. J., Slafer, G. A., Taylor, N. L., & Wittich, P. E. (2021). Addressing research bottlenecks to crop productivity. *Trends in Plant Science*, *26*(6), 607–630. https://doi.org/10.1016/j.tplants.2021.03.011

Rich, S. M., Christopher, J., Richards, R., & Watt, M. (2020). Root phenotypes of young wheat plants grown in controlled environments show inconsistent correlation with mature root traits in the field. *Journal of Experimental Botany*, *71*(16), 4751–4762. https://doi.org/10.1093/jxb/eraa201

Rossi, L. M. W., Mao, Z., Merino-Martín, L., Roumet, C., Fort, F., Taugourdeau, O., Boukcim, H., Fourtier, S., Del Rey-Granado, M., Chevallier, T., Cardinael, R., Fromin, N., & Stokes, A. (2020). Pathways to persistence: Plant root traits alter carbon accumulation in different soil carbon pools. *Plant and Soil*, https://doi.org/10.1007/s11104-020-04469-5

Schindelin, J., Arganda-Carreras, I., Frise, E., Kaynig, V., Longair, M., Pietzsch, T., Preibisch, S., Rueden, C., Saalfeld, S., Schmid, B., Tinevez, J.-Y., White, D. J., Hartenstein, V., Eliceiri, K., Tomancak, P., & Cardona, A. (2012). Fiji: An open-source platform for biological-image analysis. *Nature Methods*, *9*(7), 676–682. https://doi.org/10.1038/nmeth.2019

Scripting the Trainable Weka Segmentation . (2021). https://imagej.github.io/plugins/tws/scripting

Seethepalli, A., Dhakal, K., Griffiths, M., Guo, H., Freschet, G. T., & York, L. M. (2021). RhizoVision Explorer: Open-source software for root image analysis and measurement standardization. *AoB Plants*, *13*(6), plab056. https://doi.org/10.1101/2021.04.11.439359

Seethepalli, A., Guo, H., Liu, X., Griffiths, M., Almtarfi, H., Li, Z., Liu, S., Zare, A., Fritschi, F. B., Blancaflor, E. B., Ma, X.-F., & York, L. M. (2020). RhizoVision Crown: An Integrated Hardware and Software Platform for Root Crown Phenotyping. *Plant Phenomics*, *2020*, 3074916. https://doi.org/10.34133/2020/3074916

Seethepalli, A., & York, L. M. (2020). *RhizoVision Explorer—Interactive software for generalized root image analysis designed for everyone*. Zenodo. https://doi.org/10.5281/zenodo.4095629

Smith, A. G., Han, E., Petersen, J., Olsen, N. A. F., Giese, C., Athmann, M., Dresbøll, D. B., & Thorup-Kristensen, K. (2020). RootPainter: Deep Learning Segmentation of Biological Images with Corrective Annotation. *BioRxiv*. https://doi.org/10.1101/2020.04.16.044461

Topp, C. N., Bray, A. L., Ellis, N. A., & Liu, Z. (2016). How can we harness quantitative genetic variation in crop root systems for agricultural improvement?: Quantifying root architecture for crops. *Journal of Integrative Plant Biology*, *58*(3), 213–225. https://doi.org/10.1111/jipb.12470

Trachsel, S., Kaeppler, S. M., Brown, K. M., & Lynch, J. P. (2011). Shovelomics: High throughput phenotyping of maize (*Zea mays* L.) root architecture in the field. *Plant and Soil*, *341*(1), 75–87. https://doi.org/10.1007/s11104-010-0623-8

Tracy, S. R., Nagel, K. A., Postma, J. A., Fassbender, H., Wasson, A., & Watt, M. (2020). Crop improvement from phenotyping roots: Highlights reveal expanding opportunities. *Trends in Plant Science*, *25*(1), 105–118. https://doi.org/10.1016/j.tplants.2019.10.015

Voorhees, W. B., Carlson, V. A., & Hallauer, E. A. (1980). Root length measurement with a computer-controlled digital scanning micro-densitometer. *Agronomy Journal*, *72*(5), 847–851. https://doi.org/10.2134/agronj1980.00021962007200050035x

Wickham, H. (2016). *ggplot2: Elegant graphics for data analysis* (2nd ed.). Springer International Publishing. https://doi.org/10.1007/978-3-319-24277-4

Yu, H., & Fan, J. (2017). A novel segmentation method for uneven lighting image with noise injection based on non-local spatial information and intuitionistic fuzzy entropy. *EURASIP Journal on Advances in Signal Processing*, *2017*(1), 74. https://doi.org/10.1186/s13634-017-0509-5

Zhang, J., Zheng, T., Fu, X., Wang, W., & Huo, N. (2013). Image thresholding method based on uneven lighting. *Proceedings of the 32nd Chinese Control Conference*, *2013*, 4549–4552.

SUPPORTING INFORMATION

Additional supporting information may be found in the online version of the article at the publisher's website.